

Improved Particle Identification Using Cluster Counting in a Full-Length Drift Chamber Prototype

Jean-François Caron^{a,**}, Christopher Hearty^a, Philip Lu^a, Rocky So^a, Racha Cheaib^b, Jean-Pierre Martin^c, Wayne Faszler^d, Alexandre Beaulieu^e, Samuel de Jong^e, Michael Roney^e, Riccardo de Sangro^f, Giulietto Felici^f, Giuseppe Finocchiaro^f, Marcello Piccolo^f

^aThe University of British Columbia, 6224 Agricultural Road, Vancouver, BC, Canada V6T 1Z1

^bMcGill University, 3600 rue University, Montreal, QC, Canada H3A 2T8

^cUniversité de Montréal, 2900 Boulevard Édouard-Montpetit, Montréal, QC, Canada H3T 1J4

^dTRIUMF, 4004 Wesbrook Mall, Vancouver, BC, Canada V6T 2A3

^eUniversity of Victoria, PO Box 3055, STN, CSC, Victoria, BC, Canada V8W 3P6

^fLaboratori Nazionali di Frascati dell'INFN, Via Enrico Fermi 40, I-00044 Frascati, Italy

Abstract

Single-cell prototype drift chambers were built at TRIUMF and tested with a ~ 210 MeV/c beam of positrons, muons, and pions. A cluster-counting technique is implemented which improves the ability to distinguish muons and pions when combined with a traditional truncated-mean charge measurement. Several cluster-counting algorithms and equipment variations are tested, all showing significant improvement when combined with the traditional method. The results show that cluster counting is a feasible option for any particle physics experiment using drift chambers for particle identification. The technique does not require electronics with an overly high sampling rate. Optimal results are found with a signal smoothing time of ~ 5 ns corresponding to a ~ 100 MHz Nyquist frequency.

Keywords: cluster counting, drift chamber, gaseous ionization detector, detector, SuperB

PACS: 07.77.Ka, 29.40.Cs

Contents		2 Apparatus	4
1 Introduction	2	2.1 Prototype Drift Chambers	4
1.1 Drift Chambers	2	2.2 Amplifiers	5
1.2 Cluster Counting	3	2.3 Wire Voltages	6
1.2.1 Technique	3	2.4 Cabling	6
1.2.2 PID	3	2.5 Test Beam	7
1.2.3 Cluster Timing	3	2.6 Time of Flight	7
1.2.4 Tracking	4	2.7 Trigger	8
		2.8 Data Acquisition System	8
		3 Simulations	9
		4 Beam Test Data	9
		5 Analysis	10

*Corresponding author.

**Telephone number: +1 604 822-1445

Email address: jfcaron@phas.ubc.ca (Jean-François Caron)

5.1	Single-Cell Information	10
5.1.1	Time of Flight	10
5.1.2	Baselining and Signal Confirmation	10
5.1.3	Charge Integration	10
5.1.4	Cluster Counting	11
5.2	Track Composition	13
5.3	Combined Likelihood Ratio	14
5.4	Figures of Merit	15
6	Results	15
6.1	Charge Integration	15
6.2	Cluster Counting	16
6.3	Cluster Timing for PID	17
6.4	Dependence of PID on Gas Gain	17
6.5	Momentum	18
6.6	Dependence of PID on Window (Z-position)	18
6.7	Cables	19
6.8	Amplifiers	20
6.9	Summary of Results	20
7	Conclusions	21
Appendix A Cluster-Counting Algorithms		21
A.1	Smoothing Procedures	22
A.1.1	Boxcar Smoothing	22
A.1.2	Averaging	22
A.2	Signal above Average	22
A.3	Smooth and Delay	22
A.4	Second Derivative	22
A.5	Timeout Booster	23

1. Introduction

This paper describes the development and testing of a prototype drift chamber whose purpose is to evaluate the feasibility of a “cluster-counting” technique[1] for implementation in a high luminosity e^+e^- experiment. Cluster counting is expected to improve particle identification (PID) by reducing the effect of fluctuations in drift chamber signals. These are due to gas amplification and the fluctuation in the number of primary electrons per ionization site. There may also be improvements in tracking resolution, but this is left for a later study. The requirement

of fast electronics and larger data sizes may make the technique impractical in terms of capital costs, available space near the detector, and computing power. To date the technique has not been deployed in an operating experiment. This work demonstrates that a cluster-counting drift chamber is a feasible option for an experiment such as SuperB[2][3]. SuperB was cancelled after the experiments described in this paper, but the results are applicable to any drift chamber that is used for particle identification. The design of our prototype chambers was strongly influenced by the demands of SuperB, which are described in the Technical Design Report[4].

1.1. Drift Chambers

Drift chambers are general-purpose detectors that can track and identify charged particles[5][6]. They consist of a large volume of gas with instrumented wires held at different voltages. When charged particles move through the chamber they ionize the gas particles. The electrons from these primary ionizations drift towards the wires held at high positive voltage, while the ions drift towards the grounded wires. The sense wires are very thin ($\sim 20\mu\text{m}$), such that the strong electric field accelerates the electrons enough to cause further ionization near the sense wire. The new electrons ionize further into an avalanche, which is registered as an electronic signal on the sense wire. The amplification of the low-integer number of primary ionization electrons into a detectable signal on the wire is called the gas gain.

The energy loss of a heavy ($m \gtrsim 1\text{MeV}/c^2$) charged particle from primary ionizations depends on its speed, as given by the Bethe formula[7] and various corrections[8]. The speed measurement is combined with the independent momentum measurement from tracking, giving the particle’s mass, which is a unique identifier. To measure speed, we measure or estimate a quantity proportional to the number of primary ionizations. A traditional drift chamber accomplishes this by measuring the total ionization per unit length of the track, which is proportional to the integral of the electronic signal on the sense wires belonging to a track. The theoretical probability distribution function for the total ionization is a Landau distribution, which has an infinite mean

and standard deviation[6]. The consequence is that if one takes the average of a number of samples (e.g. 40 measurements of deposited charge in a track), the resulting distribution is non-Gaussian and is dependent on the number of samples taken. Instead of the mean of the distribution, one can use the most probable value for the total ionization. This is accessed by a truncated mean technique. Our truncated mean procedure is described in Sec. 5.2.

1.2. Cluster Counting

The conventional technique described above is sensitive to gas gain fluctuations as well as the statistical fluctuations in the number of primary electrons produced in each ionization event. Moreover, the truncated mean procedure that is typically used discards a substantial fraction of the available information. None of these disadvantages exist if the number of primary ionizations can be measured more directly.

1.2.1. Technique

The cluster-counting technique involves resolving the cluster of avalanching electrons from each primary ionization event. This is done by digitizing the signal from the sense wire in each cell and applying a suitable algorithm. The rise time of the signal from a cluster is approximately 2 ns, so electronics with sufficiently high bandwidth are required.

In principle, clusters can be detected as long as they do not overlap completely in time. This can happen irrespective of the electronics involved due to the probabilistic nature of the ionization process. Overlapping clusters are more likely for highly oblique tracks. Complex algorithms which consider signal pulse heights might disentangle even overlapping clusters, but the algorithms tested in this work do not.

An optimal algorithm would have a high efficiency for identifying true clusters and a low rate of reporting false clusters (due to noise for example).

1.2.2. PID

In traditional drift chambers using the integrated signal, the signal amplitude is determined by the convolution of the probability of primary ionization, the

number of primary electrons produced, and the variations in gas gain. This results in a long-tailed distribution that is typically dealt with by the truncated mean procedure. Conversely, if clusters are perfectly identified, then the only variation is from the primary ionization, which is a Poisson process. No cluster counts need to be discarded to allow for a proper statistical treatment. In reality some counted clusters will be missing or fake, the rate of these being caused by gas gain fluctuations, noise level, and the time separation capabilities of the electronics. The idea is that the sensitivity to these effects is small. The difficulty arises from the need to optimize an arbitrarily complex cluster-counting algorithm.

A difficulty with both charge integration and cluster counting is the presence of δ -rays[6]. These are electrons produced in primary ionizations that travel far in the gas before further ionizing, such that they create their own separate ionization cluster. The production of δ -rays at a given momentum depends only on the particle speed ($\propto 1/\beta^2$)[8]. This inflates the charge integral and the cluster count with only a weak dependence on the species of the original particle, the result is a decreased PID resolution in general. The presence of δ -rays is one of the reasons why a truncated mean is used in the charge integration method. While cluster counting is also affected by δ -rays, the effect is less pronounced, allowing all of the data to be used.

1.2.3. Cluster Timing

Any cluster-counting algorithm that uses a digitized signal is able to report not only the number of clusters in a cell, but also the arrival time of each of those clusters. In the oversimplified case of a linear and homogenous drift velocity and infinite cells, the average spacing in time between consecutive clusters would simply be proportional to the inverse of the number of clusters in the cell. In a more realistic scenario, the average spacing between clusters is useful information that is not one-to-one with the number of clusters. We can exploit the lack of perfect correlation and use the cluster timing information to further improve our ability to identify particles.

1.2.4. Tracking

For tracking, cluster counting may also improve performance, but in a much lesser degree and more subtle manner than as for PID. A traditional drift chamber uses only the arrival time of the overall signal in determining the distance of closest approach from a sense wire. Unfortunately this arrival time measurement is vulnerable to noise, gas gain fluctuations (small initial clusters may be missed), etc. If the first few clusters are resolved, then while the first cluster arrival time is still the primary datum, the second cluster arrival time can be used as a consistency check. If the second cluster arrives much too late, then the chance that the first cluster was a fake is greater, so a smaller statistical weight can be assigned to that cell when reconstructing the whole track. This paper deals only with the PID improvements and does not address tracking.

2. Apparatus

In this section we describe the prototype drift chambers that were built, the custom signal amplifiers and the various types of cables that were tested. We also describe the experimental setup in the test beam, the data acquisition system, and the devices used for external PID and triggering.

2.1. Prototype Drift Chambers

We built two nearly identical full-length (2.7 m) single-cell drift chambers, called chamber *A* and chamber *B* (Fig. 1). The only difference between the two chambers is the diameter of the sense wires: $20\ \mu\text{m}$ for Chamber *A* and 25 or $30\ \mu\text{m}$ for Chamber *B*. More details about the wires are given below.

The wire layout creates a square cell $15\ \text{mm}$ wide in a $10 \times 10\ \text{cm}$ cross-section casing (for a gas volume of $2.7 \times 10^4\ \text{cm}^3$). Figure 2 shows a cell diagram including the dimensions and wire locations. The aluminium casing of the chambers has five large windows on two sides of the cell to allow particles to enter and exit unimpeded. The windows are made of thin ($\sim 20\ \mu\text{m}$) aluminium, protected by aluminized Mylar.

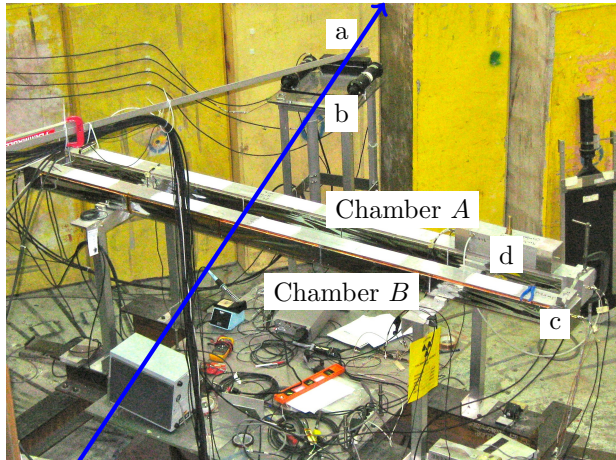


Figure 1: Photo of the prototype chambers mounted during our beam test. The far scintillator (Sec. 2.6) and additional PMTs (Sec. 2.7) are visible in the background (labelled a and b respectively). The amplifier shielding boxes (c) are on the right side of the picture. The smaller monitoring chamber (labelled d) (Sec. 2.8) is on top of Chamber B. The blue arrow shows the path of the particle beam through our prototypes and two of the scintillators.

Different amplifiers are mounted on the endplates of the drift chambers, connected directly to the sense wires. The amplifiers vary in their gain, input impedance, and bandwidth. They are described in more detail in Sec. 2.2.

We had the option of including a termination resistor to ground on the non-instrumented side of the chamber. The required termination resistance to prevent reflection of signals is $390\ \Omega$. Runs were taken with and without termination, to see the effect of reflected signals on PID performance. A circuit diagram showing our termination is in Fig. 3.

Runs were taken with chambers *A* and *B* strung with $20\ \mu\text{m}$ and $25\ \mu\text{m}$ gold-plated tungsten sense wires, respectively, and gold-plated aluminium field wires. For some later runs, chamber *B* was restrung with a $30\ \mu\text{m}$ sense wire. The wires are connected to the endplates by the same crimp-pins and feedthroughs that were used in the BaBar drift chamber[9].

The gas chosen for the test was a mixture of helium and isobutane in a 90 : 10 volume ratio. Helium was

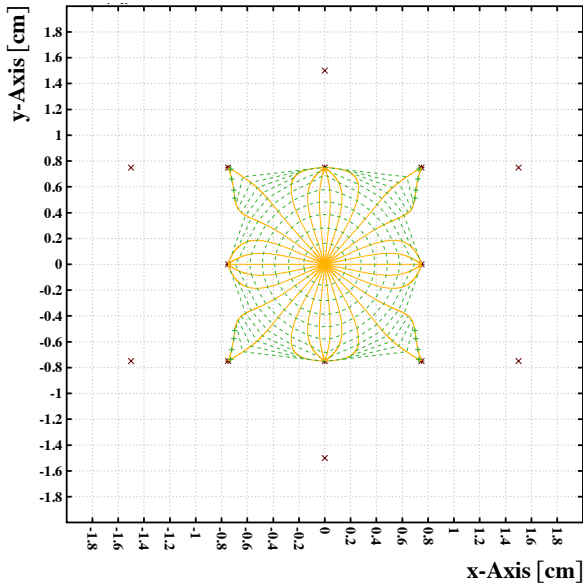


Figure 2: Garfield[11] simulation of isochrones for electron drift times in our prototypes, with 90 : 10 helium and isobutane. The isochrone intervals (dashed lines) are 50 ns. The full orange lines are the drift paths. The central point is the sense wire at high voltage, while the 8 points in a square around it are the field wires at ground. The extra 6 points outside the cell are bias wires to simulate the presence of an infinite network of cells. The wire voltages are 1820 V and 1054 V for the sense wire and bias wires respectively.

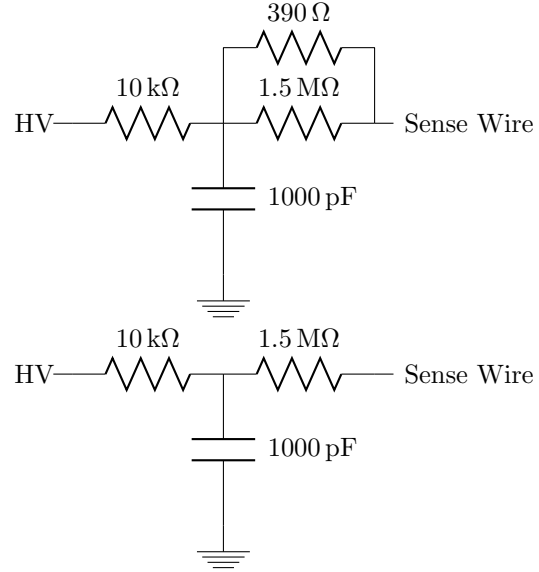


Figure 3: Circuit diagram representing the high voltage connection to the sense wire with (top) and without (bottom) termination resistor. Without the $390\ \Omega$ resistor, the signal can bounce.

chosen because it reduces the effect of multiple scattering compared to the more typical argon[10]. Multiple scattering of the charged particles is the dominant contribution to the tracking resolution at a B-factory like SuperB. In consideration of the rest of the SuperB detector, using helium reduces the number of radiation lengths represented by the drift chamber. With isobutane as the quench gas, we are able to operate the chamber with a large helium fraction, further reducing the amount of material. Helium also exhibits a lower drift velocity and ionization density, which also makes it an ideal choice for cluster counting as the incoming clusters will be less likely to overlap in the digitized signal.

The chambers are operated at room temperature and atmospheric pressure. We measured the temperature and pressure during the data taking periods, we did not use these at any level of the analysis.

2.2. Amplifiers

We used custom made amplifiers in order to achieve the bandwidth required for cluster counting. The am-

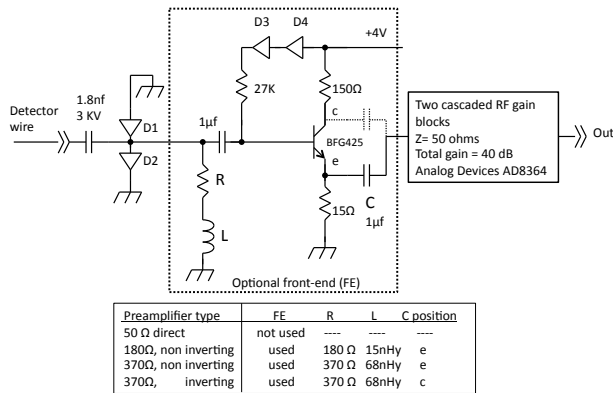


Figure 4: Simplified schematic of the amplifiers used in the experiment.

plifiers are based on the AD8354 RF gain block from Analog Devices. These have a reasonably low power consumption (~ 140 mW for the whole unit) and a bandwidth of 2.7 GHz. These devices have 50Ω input and output impedance, and a fixed gain of 20 dB. The simplest configuration that we investigated was with two AD8354s in cascade. This provides very good bandwidth performance, but the input impedance of 50Ω creates a large mismatch with the characteristic impedance of the drift chamber cells (around 370Ω) and the signal to noise ratio is not optimal. So, an emitter follower stage was added at the input, using a low noise RF transistor (BFG425). This was configured either with 370Ω input impedance, or with 180Ω , as a compromise between impedance matching and tolerance to stray capacitance. We also tried a configuration with an additional low gain ($2\times$) inverting stage (with a BFG425 transistor), having 370Ω input impedance. In this case, a single AD8354 gain block was used. The 370Ω configuration gave the best overall results. A schematic of the amplifier setup is shown in Fig. 4.

In our final analysis, only the 50Ω and 370Ω amplifiers are considered. The data runs using the 180Ω amplifiers gave signals which were of low enough quality that a full analysis was not possible.

2.3. Wire Voltages

The correct voltage settings for the guard wires in the cell were determined using the computer program Garfield[11]. The guard wire voltages are chosen to make the sensitive region of our cell behave as if it were part of an infinite array of identical cells. These voltages scale linearly with the chosen sense wire voltage.

The sense wire voltage for a given chamber and amplifier was tuned to obtain roughly equal-amplitude pulses in the final signal. This was done empirically by looking at the fraction of events on the oscilloscope (Sec. 2.8) that saturated the full voltage range. The voltage was tuned until this fraction was $\sim 15\%$.

The resulting voltage for chamber A ($20 \mu\text{m}$ sense wire) using one of the 50Ω amplifiers is 1700 V. The corresponding electric field at the wire surface is calculated by Garfield to be 217 kV/cm.

2.4. Cabling

For some of the runs we varied the type of signal cable used to connect the output of the amplifiers to the data acquisition system. We used two different types of Sub-Miniature RG-59/U cables (models 1855A and 179DT from Belden) and Miniature Coax (model 1282 from Belden), all with 75Ω impedance. The lengths were all 10 m, which is the distance between the amplifiers and digitizers for SuperB. From the signal-propagation perspective, the 1855A is a better cable than the 179DT, having less signal attenuation (34 db/100m versus 70 db/100m at 1 GHz). From the perspective of mechanical integration with the rest of the detector however, the 179DT cable would be preferable to the 1855A, being lighter, thinner, and allowing a smaller minimum bend radius (25.4 mm versus 38.1 mm).

We also took data with a header connector between the amplifier and the signal cable to simulate a connector through the real drift chamber bulkhead. The header connector has 20 pins with a 2.54 mm pin spacing. Only two pins are used in the connector to connect the ground and signal parts of an additional 30 cm 1855A cable which is inserted in our signal cable length using regular BNC connectors.

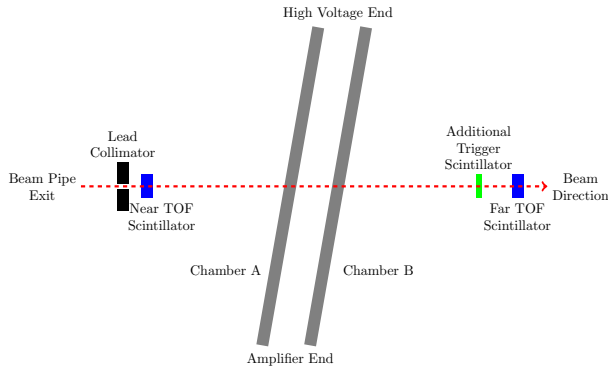


Figure 5: Schematic of beam test setup at the TRIUMF M11 facility. The distances in this schematic are not to scale, though the drift chamber proportions are correct.

2.5. Test Beam

Data were collected at the TRIUMF M11 beam[12], which simultaneously delivers positrons, positive muons, positive pions at a tuneable momentum range of 100 to 350 MeV/c. We block residual protons from upstream using a slab of polypropylene at the mouth of the beam pipe (6.35 mm thick at 210 MeV/c). We can determine the beam populations using the time-of-flight system described in Sec. 2.6.

The prototypes were mounted on a rotating and moveable table, which allowed us to take runs at different dip angles and positions along the length of the sense wires. A schematic of the beam test setup is in Fig. 5 and a photo of the test hall is in Fig. 1.

Most of the data were collected at 210 MeV/c, a relatively low momentum for a high-energy particle physics experiment. At this momentum however the Bethe formula separation of pions and muons is similar to the separation of pions and kaons at 2 GeV/c. This is confirmed by our simulations at both momenta, described in Sec. 3. High-efficiency separation of pions and kaons at 2 GeV/c is critical for high-precision measurements and reconstructions at a high-energy particle experiment like SuperB.

2.6. Time of Flight

An external time of flight (TOF) system was used to identify the particles independently of the pro-

totypes. The beam’s momentum spread is small enough that a histogram of the TOF shows distinct peaks corresponding to the species of the particles in the beam. The TOF system consists of two counters ~ 4 m apart, one upstream of the prototypes and one downstream (Fig. 5). The counters are $12.7 \times 12.7 \times 220$ mm BC-404 scintillators each read out by two Burle 8501-1 64-channel micro-channel plates (MCPs), one on each end of the scintillator block. The scintillators are roughly the same size as the beam spot. The MCPs have $25 \mu\text{m}$ pores. Each of the 64 channels in the MCPs have an active region of 6×6 mm. We gang together four of the channels to form one combined signal. This signal from each MCP goes to an Ortec 935 constant-fraction discriminator (CFD) with no pulse height correction applied. Each is then delayed by a given time in order to separate the pulses, then they are combined and recorded in a single channel of our oscilloscope.

The signals from the MCPs are used as part of the trigger. Additional signals from photomultiplier tubes are used and are described in Sec. 2.7.

The unscaled TOF is obtained by determining the arrival time of each pulse from the MCPs as recorded by the oscilloscope. The first two pulses are from the two ends of the upstream counter, while the following two are from the downstream counter. These pairs are averaged, then the difference is taken. There are arbitrary delays associated with the MCP signals, so the TOF quantity is scaled to be physically meaningful. A run is chosen and a histogram of the TOF quantity is made, where the positrons, muons, and pions are clearly resolved as Gaussian peaks. We fit the positron peak with a Gaussian distribution. The beam momentum is high enough that the positrons may be treated as moving at the speed of light, and the actual distance between the two counters is well-measured.

We were able to achieve TOF resolutions of ~ 60 ps per MCP. For a 210 MeV/c beam (Fig. 6) the separations of the Gaussian peaks are greater than the 3σ ranges used to identify particles in our track composition process described in Sec. 5.2. A sample trace of the actual TOF signal is shown in Fig. 7, where the first four pulses are from the MCPs.

We fit the TOF distribution with the sum of three

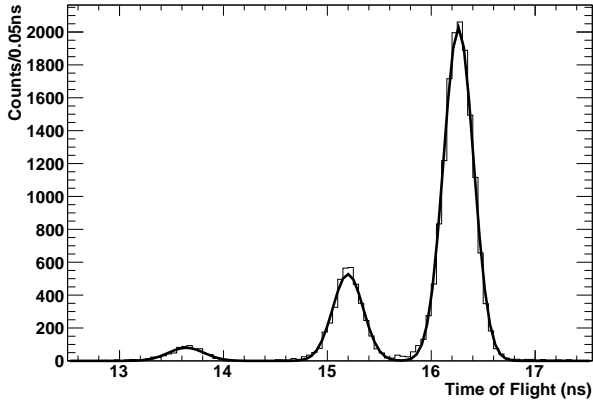


Figure 6: Time-of-flight histogram for a run at 210 MeV/c beam momentum. The three peaks correspond to positrons, muons, and pions, in increasing TOF order. The fit is to the sum of three Gaussians.

Gaussians and count how many particles are within 3σ of each peak. For the run shown in Fig. 6, we find that of all the physical triggers 3.8% are positrons, 20.5% are muons, and 75.7% are pions.

2.7. Trigger

The TOF signals are also used as part of the trigger system for the oscilloscope. It was noted that with only the upstream and downstream counters, many events contained no signals in the drift chambers (i.e. oscilloscope traces with just normal noise, no clusters). In addition, the TOF histogram showed six peaks, though only three were expected. The six peaks appeared to be in two similar groups, shifted in TOF value. The conjectured origin of the higher-TOF valued population was beam particles passing through the upstream counter but angled downwards, scattering off of the metal table, then passing through the downstream counter, bypassing the chambers entirely and taking a longer path.

A third scintillator strip 3 mm thick was placed between the prototypes and the downstream counter (Fig. 5), instrumented with photomultiplier tubes. The coincidence of the three (upstream, downstream, strip) was required for a physical trigger. This additional requirement removed the extraneous TOF population and many of the events with no drift cham-

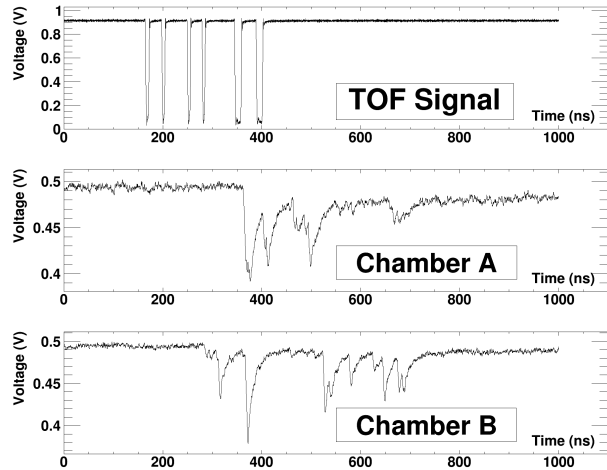


Figure 7: Oscilloscope traces for a run at 210 MeV/c beam momentum. The first is the TOF signal, with four initial pulses from the TOF MCPs, and two additional pulses from the extra trigger PMT. The TOF value identifies this particle as a pion. The second and third traces are from prototypes A and B, respectively. The cluster structure is clearly evident in these signals.

ber signals. Part of the trigger signal can be seen in Fig. 7 in the upper trace. The third scintillator was not digitized and thus is not visible in the figure.

The coincidence rate is ~ 30 Hz, while the signal rate on the upstream counter without requiring coincidences ranges from a few kHz to tens of kHz, depending on beam line settings. We also introduced an asynchronous trigger based on a pulse generator whose frequency was tuned to $\sim 15\%$ of the total trigger rate. These asynchronous triggers are uncorrelated with real beam events. They provide a sample of empty events for monitoring and measuring baseline voltages and noise levels during the run.

2.8. Data Acquisition System

Our data acquisition system consisted of a LeCroy WavePro 740Zi, an oscilloscope with 4GHz bandwidth. Data were written to an external USB hard disk in a proprietary binary format and then converted into ROOT[13] files for analysis. The oscilloscope writes one file per active channel per trigger. We used one channel for the time-of-flight system and

one channel for each prototype sense wire, meaning we had three small files written per trigger. Each channel read 20002 samples with 50 ps spacing, for a trace duration of $\sim 1 \mu\text{s}$. The biggest bottleneck was the filesystem (Microsoft NTFS), which does not perform well with directories having tens of thousands of files. The overall rate of events written to disk was $\sim 12 \text{ Hz}$.

We used the MIDAS[14] data acquisition system to automatically record temperature and atmospheric pressure as well as the current in a small monitoring chamber. The monitoring chamber was connected in series with the primary chambers on the gas line, and was exposed to an ^{55}Fe source. The monitoring chamber wire voltages were held fixed, allowing us to monitor the gas and environmental conditions by tracking changes in the gas gain.

3. Simulations

We used a gaseous ionization detector simulation package called Garfield[11] to simulate tracks through our prototypes. We did not simulate the electronics chain and the data acquisition system, but we are able to get predicted charge depositions and cluster counts for our specific gas mixture and wire configuration.

The charge deposition is not reported directly, but is proportional to the energy lost by charged particles passing through the gas. It is plotted in Fig. 8 for muons, pions, and kaons. The momentum scale is chosen to illustrate the fact that the difference in energy loss between pions and muons at $\sim 200 \text{ MeV}/c$ is similar to that between pions and kaons at $\sim 2 \text{ GeV}/c$ (Sec. 2.5).

The number of primary ionizations is reported directly by the simulation software and can be treated as a “true” number of clusters. It does not depend on the choice of electronics, algorithms, and it does not count δ -rays (Sec. 1.2.2). The distribution of primary ionizations for muons, pions and kaons is shown in Fig. 9 and also shows the similarity between muon-pion separation at our beam momentum and pion-kaon separation at higher momenta. It is also important to point out that the absolute number of

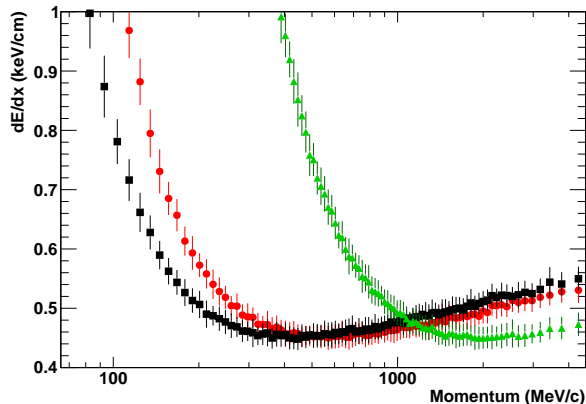


Figure 8: Garfield simulation of the energy loss by a charged particle crossing 40 cells of a 90:10 mixture of helium and isobutane. The black squares, red circles, and green triangles represent muons, pions, and kaons, respectively. The marker position is the 70 % truncated mean energy loss, while the vertical error bar on each marker is the RMS of the truncated mean.

clusters for muons and pions at $210 \text{ MeV}/c$ approximately mirrors that of pions and kaons at $2 \text{ GeV}/c$, not just the difference. The absolute value is important because it is related to our ability to actually resolve the clusters.

4. Beam Test Data

The data were taken during August and September 2012. Approximately 200 runs of 30000 events were acquired. A run is a contiguous data-collection period during which no setup parameters are changed. On average, 15% of the events were from asynchronous triggers and 10% of the physical triggers did not leave signals in the prototypes.

Various parameters were changed from run to run. These were: the sense wire voltages, amplifiers, signal cable types, beam momentum, angle of incidence of the beam with the chamber, beam position along the sense wire length and presence of a proper termination resistor on the sense wire. In the end, many runs turned out to be recorded using unsuccessful amplifier prototypes and could not be used for a detailed

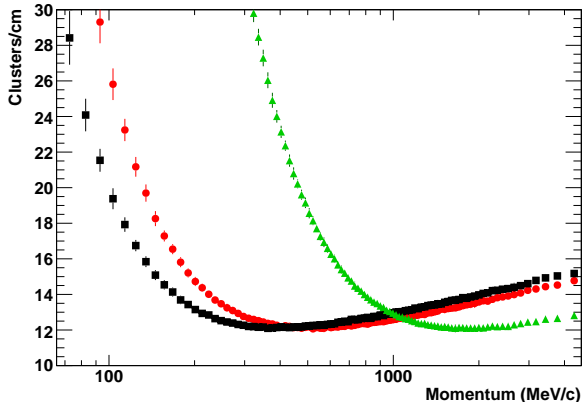


Figure 9: Garfield simulation of charge clusters produced by a charged particle crossing a 90:10 mixture of helium and isobutane. The black squares, red circles, and green triangles represent muons, pions, and kaons, respectively. The marker position is the average number of clusters, while the vertical error bar on each marker is the RMS.

analysis. This analysis uses 20 runs, for a total of 633050 recorded events.

5. Analysis

The analysis of the test-beam data is performed in two steps, both of which are done offline (after the data for that run has been fully collected). The first step involves analyzing the signals (voltage as a function of time) from the three oscilloscope channels. The first channel is connected to the time-of-flight (TOF) system, with voltage pulses corresponding to a particle crossing the scintillators before and after the drift chambers. The second and third oscilloscope channels are connected to the amplifiers on the sense wires of the two drift chambers.

The second step of analysis involves constructing multi-cell “tracks” from the single-cell events using a composition process. Single-cell events are taken from the same run, same chamber, and having a TOF consistent with the same particle type. Forty of these are used to build up a track as if it were traversing a full SuperB-size drift chamber (Sec. 5.2).

5.1. Single-Cell Information

This section describes in detail the first stage of analysis in which we deal with single-cell events. The time-of-flight is measured, the signal is adjusted for baseline drift and basic quality controls are imposed. In this stage we also perform the charge integration and use cluster-counting algorithms to count clusters on the drift chamber signals.

5.1.1. Time of Flight

The time-of-flight is determined by applying a simple threshold-over-baseline algorithm to the oscilloscope trace from the channel connected to our scintillator MCPs and PMTs. A valid TOF signal consists of four identified pulses, while an asynchronous trigger has zero pulses. Events with one, two, or three TOF pulses are rejected, and represent the small fraction of events from asynchronous triggers with a pulse in one of the TOF counters.

5.1.2. Baselining and Signal Confirmation

The baseline voltage for each drift chamber is simply the average voltage of the entire signal from the previous asynchronous trigger. The RMS deviation from this baseline is also measured. The mean of these RMS deviations is ~ 2 mV. Signals from physical triggers have amplitudes on the order of hundreds of mV above the baseline.

The real particle events are tested for the presence of an actual signal by a threshold algorithm, where the baseline and threshold levels are determined by the previous asynchronous trigger measurements. Real particle events that have no signal in the chambers are rejected. These are from events where a real particle crossed the scintillators, but either missed one or both drift chambers, or did not interact within them.

5.1.3. Charge Integration

A charge integration is performed for the remaining asynchronous and physical events, starting at the time of the threshold crossing mentioned in 5.1.2 (or at an arbitrarily chosen time for asynchronous events), integrating for a fixed duration. The distribution of start times for a sample run is shown

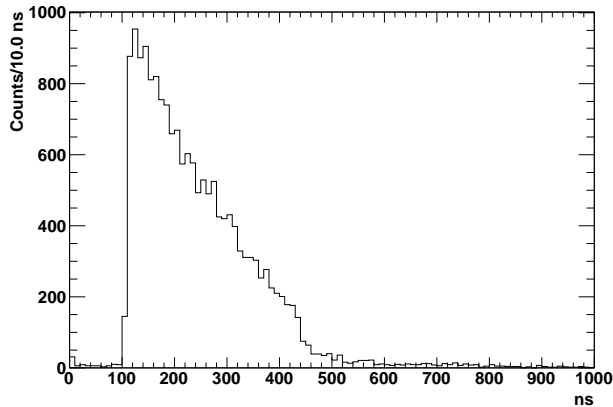


Figure 10: Time at which the charge integration begins in Chamber A for a run at 210 MeV/c.

in Fig. 10. If the duration is too short, then some pulses may be missing or the tail of the last pulse may be clipped. If the duration is too long, then unnecessary noise is also integrated, reducing the resolving power of the charge measurement. Different equipment combinations give different pulse tail decay times, so the duration must be optimized empirically. A typical optimal value is ~ 600 ns, as shown in Fig. 11. The optimization of the integration time is described in Sec. 6.1.

From the integrated charge we subtract a pedestal calculated from the previous asynchronous trigger. This pedestal is a charge integration with the same integration time, but a fixed starting time. The result is a baseline-subtracted charge, which should have a smaller systematic error than the raw charge integral. The distribution of integrated charges for physical triggers and asynchronous triggers is shown in Fig. 12. The physical triggers are shown separately for each species in Fig. 13.

5.1.4. Cluster Counting

Cluster-counting algorithms can vary in complexity, efficiency, and in their rate of reporting fake clusters. Here we briefly describe the various algorithms, but precise definitions can be found in Appendix A.

The algorithms involve two forms of smoothing of the oscilloscope traces (Fig. 14). The first is a “box-car smoothing” where each sample is replaced with

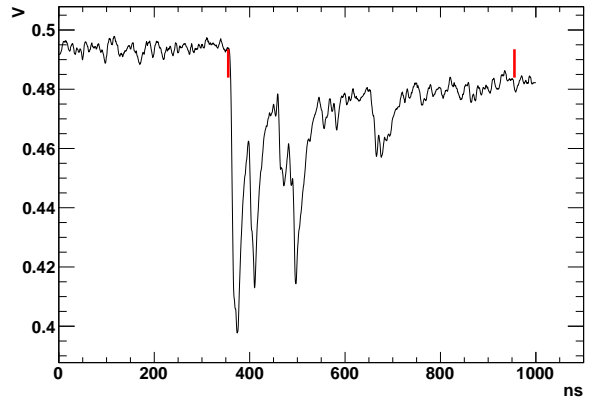


Figure 11: Sample event in chamber A showing 600 ns integration time.

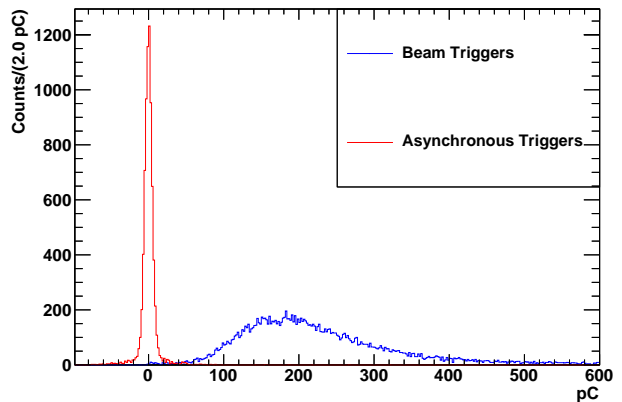


Figure 12: Baseline-subtracted charge distributions as identified by the time-of-flight system. The sharp peak on the left is from asynchronous triggers (with no particles in the prototypes), while the broader peak in the middle is from physical triggers with all particle species combined.

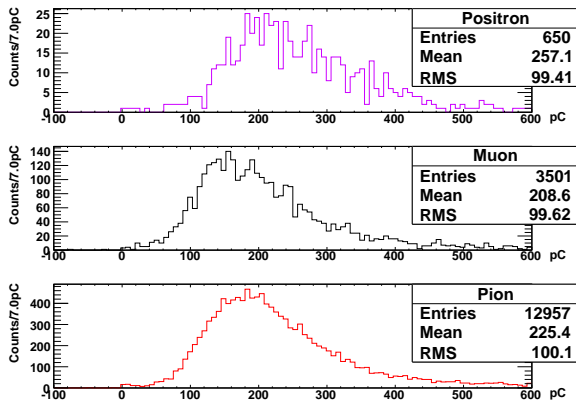


Figure 13: Baseline-subtracted charge distributions for each particle species at 210 MeV/c. Note that the sample mean and RMS values indicated in the figure are not representative of the underlying distribution since it does not have well-defined moments.

the average of itself and the $n - 1$ previous samples. The second is a true averaging procedure, where the number of points in a trace is reduced and each point is the average of n points.

All of the algorithms involve some kind of transformation of the smoothed signal, and a threshold-crossing criterion. The transformed signals for the various algorithms are shown in Fig. 15. One of the most basic cluster-counting algorithms is the “Threshold above Average”. It subtracts the non-smoothed signal at time t from the boxcar-smoothed signal at time $t - 1$, then applies a threshold.

A more general algorithm (of which the previous is a special case) is the “Smooth and Delay” algorithm. It involves smoothing two copies of the signal by different amounts, delaying one of the copies by a certain number of frames, then taking the difference and applying a threshold. This algorithm has four parameters, and is thus more difficult to optimize.

The two algorithms above essentially implement a first-derivative method. We also implemented a second-derivative method. This one uses the true averaging procedure rather than the “boxcar smoothing”. The first derivative is first calculated by taking the difference between consecutive smoothed samples. The second derivative is then calculated by tak-

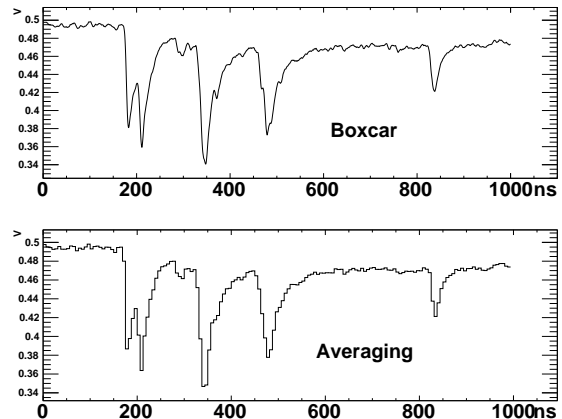


Figure 14: The two smoothing algorithms used, each smoothing over 125 frames of 50 ps width, for a smoothing width of 6.25 ns. This event is the same as shown in Fig. 11

ing the difference between consecutive first derivative values. Each time, we divide by the time interval represented by a sample, to keep the units consistent. The number of clusters counted using the second derivative is shown for each particle species in Fig. 16.

All of the threshold algorithms in principle trigger on the leading edge of cluster signals. However it is noticeable that real cluster pulses have a very sharp leading edge (approximately 3 ns) and a slower decaying trailing edge (approximately 100 ns). Fake clusters are more symmetric, returning to the baseline voltage faster than the signal from a real cluster. Thus an algorithm was devised that takes cluster candidates from the above algorithms, but requires the pulse to last a minimum duration in order to be confirmed. Pulses that return to baseline too quickly are discarded as fake clusters. This “timeout booster” allows the use of smaller thresholds, which while increasing the efficiency of finding real clusters also admit more fakes. The timeout criterion removes most of the fakes but keeps the real clusters.

As mentioned before, each of the cluster-counting algorithms can return not only the number of clusters, but the actual time at which each cluster was found. We investigated the use of this information, in the form of an average time separation between

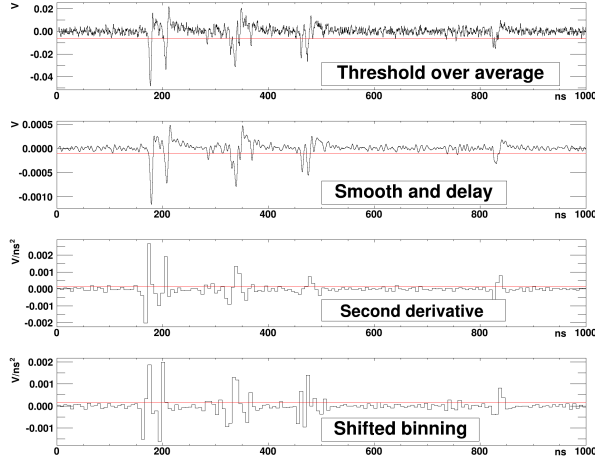


Figure 15: Illustration of the quantity on which a threshold is applied in the various cluster-counting algorithms. Each uses a set of parameters (smoothing width, threshold level) that were optimized for this run. The threshold level is indicated by the red horizontal line. The last image is the same as the second derivative, but with the binning shifted, to show that some clusters can be hidden by the binning (e.g. around 480 ns). This event is the same as shown in Figs. 11 and 14

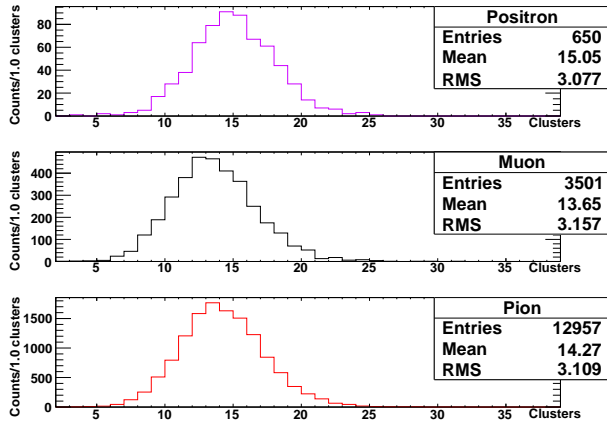


Figure 16: Number of clusters found for each species as identified by the TOF system. This is for a 210 MeV/c run using the second-derivative algorithm.

clusters in each cell.

5.2. Track Composition

The prototypes have only a single cell. The traditional method of identifying particles using the truncated mean requires many cells forming a track. Thus we construct tracks from the single-cell events.

To compose a track for a given species of particle, we select (with replacement) random single-cell events that have been identified with the time-of-flight information. We positively identify particles with TOF values within 3 standard deviations of the central values of the three Gaussian peaks corresponding to the particle species. For a typical run with e.g. 3500 single muon events, the number of possible muon tracks is astronomical ($\sim 10^{94}$), and the likelihood of a given track being composed of multiple copies of the same single-cell event is low ($\sim 1\%$). We also form empty tracks by combining the signals from asynchronous events.

The information from each event is combined to form the track information. The track information is the particle species, total number of clusters found per cm of track, and the truncated mean of the charge integrals from each cell. The truncated mean is performed by sorting the list of charge integrals and taking 70% of the values starting from the beginning of the list. The value of 70% was roughly optimized to give better separation, for comparison 80% was used in BaBar[9]. The SuperB drift chamber design has 40 layers. Thus we use 40 events from our single-cell prototypes events to create a composed track. The 70% truncated mean was thus done by rejecting the largest 12 integrated charge values from the cells.

In the case of tracks formed from asynchronous events, the list is not sorted, since these values are already Gaussian, but still the same fraction of values is discarded. The distribution of truncated mean charge and clusters for the composed tracks is shown in Figs. 17 and 18, respectively.

We also form the track-wise average time separation between clusters by doing a weighed average of the cell-wise average cluster separation for the events in the track. The weights are the number of clusters in the cells.

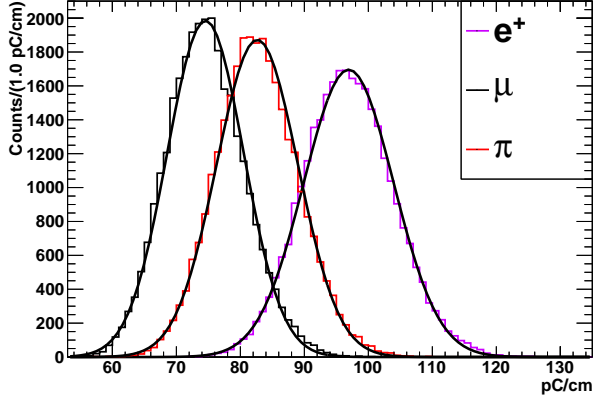


Figure 17: Truncated mean of charges (dE/dx) in composed tracks. This is using events from the same run as Fig. 13. The three peaks from left to right are from muons, pions, and positrons, respectively. Here the particle populations are equal, as we compose an equal number of tracks for each species.

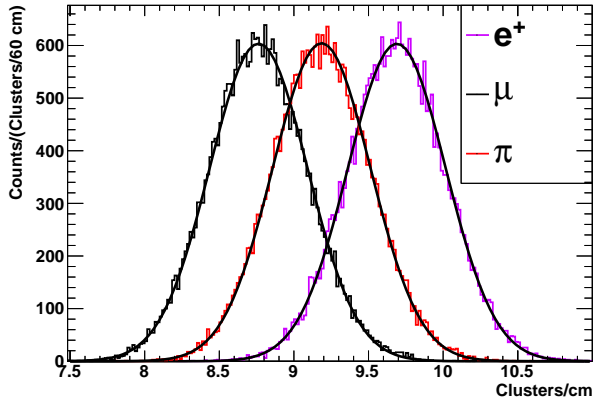


Figure 18: Number of clusters per cm in composed tracks. This is using events from the same run as Fig. 16 and using the second-derivative algorithm. The three peaks from left to right are from muons, pions, and positrons, respectively. Here the particle populations are equal, as we compose an equal number of tracks for each species.

It is worth noting that the relative separations of the muon and pion peaks shown in Figs. 17 and 18 are very different. For the truncated mean of the integrated charges, the relative separation between the peaks (difference in the location of the peaks, divided by the average of the two) is $\sim 10\%$, while for the cluster counting it is $\sim 5\%$. Naïvely this should mean that the cluster counting technique is less effective. However because the widths of these peaks is also very different, the two techniques turn out to be of comparable power (Fig. 19).

5.3. Combined Likelihood Ratio

In order to combine the information from the truncated mean and the cluster count, we form likelihoods based on fits to the two quantities. These quantities are reasonably Gaussian (for non-empty tracks), so we fit them with Gaussian distributions $G_{s,k}$, for particle species s and measured quantity k . For a given track, the likelihood of the track coming from a particle s is found by evaluating the product of the fitted distribution functions for both k s at the measured values. Thus if the measured truncated mean charge for a track is q and the clusters per cm of track are n , the combined likelihood is

$$L_s(q, n) = G_{s,\text{charge}}(q) \times G_{s,\text{clusters}}(n). \quad (1)$$

This combined likelihood ignores any correlation between the two quantities. The correlation is indeed non-zero but is somewhat weak (~ 0.3). Possibly combined likelihood models which make use of the correlation would be more effective, but we did not investigate this.

As mentioned in Sec. 2.5, the ability to identify muons and pions at $\sim 210 \text{ MeV}/c$ is our proxy variable for the performance of the prototypes. Thus we form a ratio of the combined likelihoods of being a muon and pion:

$$R(q, n) = \frac{L_\mu(q, n)}{L_\mu(q, n) + L_\pi(q, n)}. \quad (2)$$

This quantity's distribution is peaked at 0 for real pions and at 1 for real muons. A cut can be made

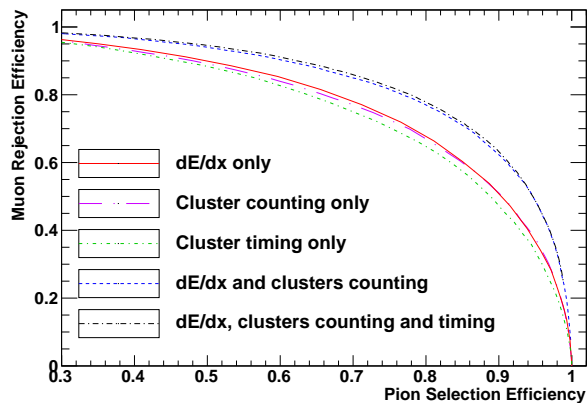


Figure 19: Efficiency graph for a run at 210 MeV/c, the same run as earlier figures. The cluster counting is done using the second-derivative algorithm. The upper two curves nearly coincide and are the efficiencies when cutting on the combined likelihood ratios. One combines the truncated mean, cluster count, and cluster separation, the other only truncated mean and cluster count. The lower three curves are the efficiencies when one cuts directly on the truncated mean, cluster count, or cluster separation quantities.

that maximizes the separation according to some figure of merit. A typical way to demonstrate the performance is by making a rejection-selection efficiency plot. Consider the fraction of real pions that would also be identified as pions by the cut on R , and the fraction of real muons that would not be identified (that is, rejected) as pions by the cut on R . We can thus make a parametric plot of muon rejection efficiency on the vertical axis and pion selection efficiency on the horizontal axis, with the parameter being the chosen R cut value (Fig. 19). Similar efficiency graphs can be made for cuts directly on the physical quantities of charge and cluster counts.

5.4. Figures of Merit

The efficiency graphs are a good way to represent the performance of a particular setup, but they are two-dimensional and difficult to include in summaries. Thus we construct figures of merit in order to quantify the performance of an equipment choice or algorithm. A convenient method is to set a given background rejection level and state the corresponding signal efficiency. In the muon rejection and pion

selection plot, one may thus find the muon rejection efficiency corresponding to 90% pion selection efficiency, or vice-versa. These figures of merit are easy to interpret physically and correspond to how detector performance is typically quantified in past experiments.

An alternative figure of merit turns out to better differentiate between algorithm parameter choices, but has a much less intuitive physical meaning. It is the maximum excursion on the muon rejection and pion efficiency plot from the origin of the graph. The curves on the graph approach $(0, 1)$ and $(1, 0)$ in the limits of R cut values of 0 and 1 respectively, but the curves can lie above that inscribed by a circle of unit radius. The length of the longest straight line joining $(0, 0)$ and the efficiency curve is taken as the figure of merit. In certain cases the performance is bad enough that the lines lie below that inscribed by a circle, in this case the alternative figure of merit is not meaningful, as it is identically 1.

All three figures of merit can be shown to be equivalent, in the sense that local maxima and minima lie in the same regions of parameter space. The maximum-excursion-from-origin figure gives better separation for those runs where it is meaningful (the majority). It is used for the optimization of algorithms, but the results are presented using the more intuitive figure of merit of pion selection efficiency at 90% muon rejection.

6. Results

In this section we present the results of varying the cluster-counting algorithms, gas gain, various chamber positions, and other equipment choices.

6.1. Charge Integration

The time over which to integrate a signal in order to capture the charge deposition on the wire was determined empirically. In principle the optimal value varies from run to run depending on gas gain, dip angle of the beam, and window position, but we wish to compare runs at different settings. Thus we look at the figure of merit for many different runs and choose a suitable compromise (Fig. 20). As it turns out, the

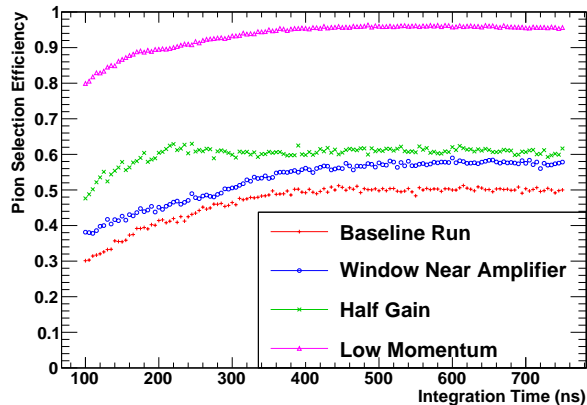


Figure 20: Pion selection efficiency using dE/dx only for several runs as a function of charge integration time. The baseline run is at a window 1883 mm from the amplifier, 210 MeV/c and using nominal gain as calculated by simulations. The low-momentum run is at 140 MeV/c. All the runs use the extra termination resistor.

performance does not vary strongly as a function of integration time once the time is suitably long. We choose an integration time of 600 ns for the rest of the study.

6.2. Cluster Counting

The various cluster-counting algorithms have parameters that must be tuned empirically. By iterating this procedure many times using the same run, a “map” of the figure of merit can be created in the algorithm parameter space, the maxima of which are optimal values for the algorithms (Fig. 21). While the figure of merit includes the PID performance from dE/dx and cluster counting, the dE/dx contribution is essentially constant even with the randomness introduced by the track composition process.

The optimal parameters vary from algorithm to algorithm and depend on the run used to optimize the parameters. In an operational experiment, only one set of parameters can be chosen, so some compromise will be necessary. Nevertheless, to compare the algorithms themselves, we may compare the performance of each algorithm when optimized on the same data run.

The chosen run has the following parameters: 10 degree dip angle, window 1883 mm from the ampli-

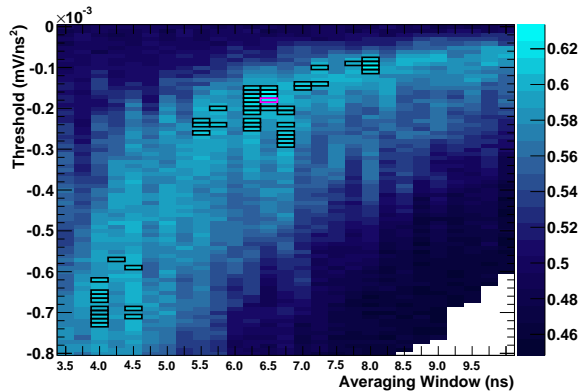


Figure 21: Example performance “heat map” for the second-derivative algorithm using a run at 210 MeV/c. In this case, the optimal parameters are an averaging window of ~ 6.5 ns and a threshold of ~ -0.16 mV. The black rectangles are the highest-performance regions, the magenta is the single best.

fier, and $20 \mu\text{m}$ sense wire. A 370Ω inverting amplifier and 1855A Sub-miniature RG59/U signal cable with no extra connector are used. The beam momentum was 210 MeV/c. A total of 30784 triggers were recorded of which 7720 are asynchronous, and 680, 3649, and 13579 are positively identified as positrons, muons, and pions respectively. The remainder have TOF values more than 3σ away from the peaks or have no signal in the chamber.

The dip angle of 10 degrees was chosen rather than 0 in order to avoid space charge effects. The avalanches produced on the wire from the passage of a particle at zero degrees occur all in the same gas volume near the wire. This can affect the overall results and essentially makes 0 degrees a “special” angle. In an operating e^+e^- collider experiment the fraction of tracks suffering from space charge effects is negligible.

We explored a variety of algorithms, which are described in detail in Appendix A. Each has some kind of threshold as one of the parameters, and some smoothing or averaging duration. A common feature is that the optimal smoothing or averaging duration is ~ 5 ns, which indicates that extremely high sampling rate and bandwidth are not necessary to improve PID with cluster counting. The

Table 1: Summary of optimal parameters for the various cluster-counting algorithms. The algorithms labelled *A*, *B*, *C*, *D*, and *E* are “Signal above Average”, “Smooth and Delay”, “Signal above Average with Timeout”, “Second Derivative”, and “Second Derivative (Two Passes)”, respectively. The threshold is given with the appropriate units for that algorithm, and τ is the smoothing or averaging time in nanoseconds. Algorithm *B* has in principle two smoothing times, but the optimal value has them equal. The additional parameter Δ_t for the algorithms *B* and *C* are the delay and the timeout, respectively. The figure of merit ϵ_π is the pion selection efficiency for 90% muon rejection.

Algorithm	Threshold	τ (ns)	Δ_t (ns)	ϵ_π
<i>A</i>	-6.5 mV	3.5		0.62
<i>B</i>	-0.1 mV	2.75	3.75	0.64
<i>C</i>	-3.0 mV	3.5	4.25	0.62
<i>D</i>	0.16 mV/ns ²	6.5		0.64
<i>E</i>	0.15 mV/ns ²	6.25		0.64

smoothing times correspond to Nyquist frequencies of ~ 100 MHz. Our amplifiers have much higher bandwidth than this (Sec. 2.2), so using amplifiers with smaller bandwidth but better signal-to-noise ratios should improve overall performance.

In Table 1, the figure of merit is the pion selection efficiency for 90% muon rejection. Here and in later plots, it is difficult to give a good estimate of the systematic uncertainty as many factors were not taken into account. For example the temperature of the gas in the chamber plays no role in our calculations, though the temperature did change during the data taking period. The track composition process involves drawing random numbers, so a contribution to the uncertainty from this can be estimated by composing multiple sets of tracks and seeing the distribution of results. Running the code 100 times yields an RMS deviation from the mean of ~ 0.05 . The mean is what is reported in Table 1.

In the table, only algorithm *C* uses the “Timeout Booster” technique. We also tried applying the technique to the other algorithms, but it was noticed that if the algorithm already has reasonable performance, the improvement from the timeout is negligible. Indeed the optimal timeout duration for the “Smooth and Delay” algorithm is zero, yielding the same performance as the bare algorithm.

Overall the best algorithm is the two-pass second

derivative algorithm, but it is only marginally better than the other algorithms. The difference is less than the typical variation due to the track composition process.

It is fortuitous that even the simple algorithms have good performance, as they are reasonable to implement using a field-programmable gate array (FPGA) or even analog hardware.

In some sections that follow, the PID performance with optimized cluster counting refers to the use of a cluster-counting algorithm where the parameters were chosen to give the best figure of merit for that run. The optimal parameters vary from run to run, so in each case, we also run the algorithm on a given run using parameters that were optimal for a set of other runs. The other runs each vary in only a single parameter: the window, the HV settings, and the momentum. The average performance using these non-optimal parameters is labelled “sub-optimal cluster counting” in later figures.

6.3. Cluster Timing for PID

In each cell, we take the average of the time intervals between consecutive clusters. In the track composition process, we form a weighted average of the cell-wise averages, with the weights given by the number of clusters in each track. The resulting quantity gives a reasonable separation for each particle type (Fig. 22).

Unfortunately the performance is not as good as either the traditional charge integration or cluster counting (Fig. 19). In addition, if we form a tripartite combined likelihood, the improvement relative to the bipartite charge integration and cluster counting combination is negligible. Given the increased computational complexity of calculating the average separations, it is unlikely that the timing information will be useful for PID purposes in a real particle physics experiment.

6.4. Dependence of PID on Gas Gain

The gas gain of the prototypes depends on the choice of sense wire voltage and on the gas. We tested only one gas, a mixture of helium and isobutane in a ratio of 90 : 10. A nominal voltage was selected

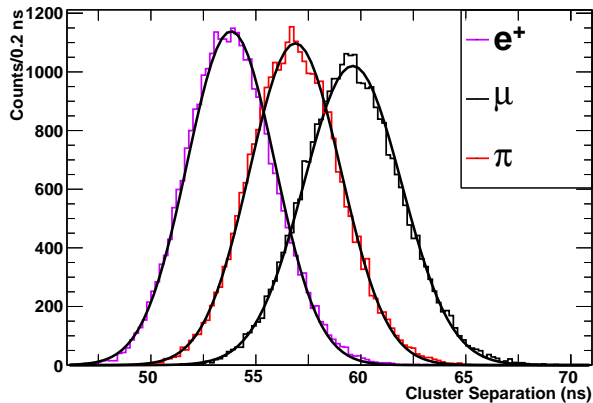


Figure 22: Track-wise weighed average of time intervals between clusters, in 50 ps units for each particle species. This is a run at 210 MeV/c. The three peaks from left to right are from positrons, pions, and muons, respectively

as described in Sec. 2.3. The actual gas gain for our gas mix and voltages is on the order of 10^5 , measured offline using an ^{55}Fe source. The procedure aims to obtain oscilloscope signals with roughly the same amplitude with all the amplifiers. The dependence of gas gain on sense wire voltage is approximately exponential[15]. In our case a ± 60 V change corresponds to a doubling or halving of the gas gain. The resulting performance after doubling and halving the gain is shown in Fig. 23.

Previous to the experiment, the intuitive notion was that higher gas gains would be better, since the signals would stand out more from the random noise on the chamber wires. It appears however that this is not the case and that indeed better PID performance can be obtained at lower gas gains. Lower performance at higher gas gains is either due to gas effects (e.g. space charge) or to the amplifiers. We did not explore the even lower gains where the performance is expected to decrease again. Data runs using other amplifiers with different gain do show the eventual decrease (Sec. 6.7), so the optimal voltage is not too far from that shown in Fig. 23 (within ~ 100 V).

When choosing a gas gain for an experiment the most important features are more often the tracking performance, ageing issues, and operational issues. This is more likely to influence the choice of specific

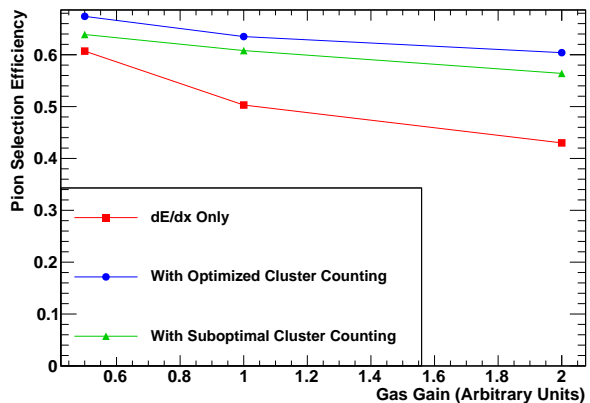


Figure 23: Variation in PID performance at the three gas gains that were explored. This is a run at 210 MeV/c using an inverting 370Ω amplifier.

gain, regardless of the PID performance. However, if PID performance is also highly valued, lower gains should be explored.

6.5. Momentum

As shown in Fig. 24, the difference of ionization between pions and muons is greater at lower momenta. This is in agreement with theoretical expectations and simulations. As expected, the improvement from adding cluster counting is most noticeable at the momentum where the overall performance is worst, making the detector response more uniform.

6.6. Dependence of PID on Window (Z-position)

The prototypes have five windows at five thin aluminium positions along their 2.7 m length. The reference point is chosen to be the amplifiers, so the high-voltage connectors at the other end of the chamber are at 2700 mm. The centres of the five windows are 283, 816, 1349, 1883 and 2415 mm from the amplifiers.

Most tests were performed at the windows 1349 and 1883 mm from the amplifiers, but a sequence of runs was taken to determine the effect of the signal propagating along the sense wire. The sense wire voltages were chosen as described in Sec. 2.3 at the middle position, but left unaltered for the other windows in the sequence. Thus the oscilloscope and am-

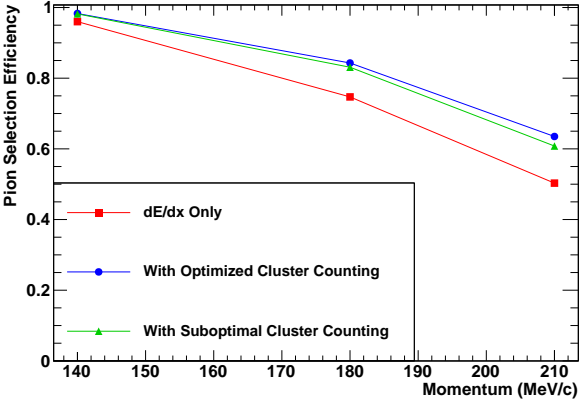


Figure 24: Variation in PID performance with momentum. These three runs all use the same amplifier with $370\ \Omega$ input impedance.

plifier saturations may change as a function of beam position.

The tungsten wire is very thin and has a non-negligible DC resistance ($421\ \Omega$ for the $20\ \mu\text{m}$ diameter wire), so it was expected that the performance would be better at the windows closer to the amplifiers. Indeed the runs taken at the two windows closest to the amplifiers have slightly higher efficiencies (Fig. 25) than at the two furthest windows, but the difference is not large. The variation for this small data set is also not monotonic, the second-closest window to the amplifiers shows inexplicably better performance than the closest.

6.7. Cables

As mentioned in Sect. 2.4, we tested two different cable types, and the effect of adding an additional header connector to simulate needing to feed through a bulkhead. Unlike the previous sections, we did not compare the performance of the cluster-counting algorithms using parameters optimized on the single run with non-optimal parameters. Thus the individual performance numbers may be optimistic, but the comparison between cable types can still be done. In Fig. 26 we show the result from several runs using an amplifier with $50\ \Omega$ input impedance. The low gain columns have the Chamber A sense wire voltage at $1820\ \text{V}$, while the high gain columns are at

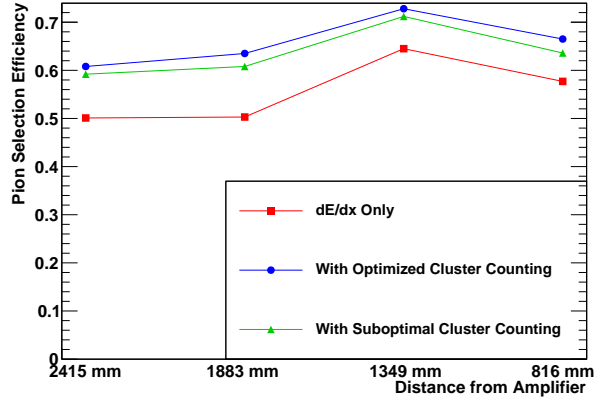


Figure 25: Variation in PID performance at the different windows of the prototype. These runs all use the same amplifier with $370\ \Omega$ input impedance.

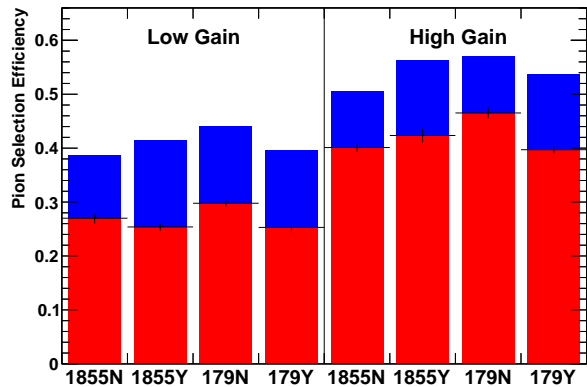


Figure 26: Variation in PID performance using different cable types. The red is the performance using charge integration only, the blue on top is the additional performance gain from combining charge integration and cluster counting. All the runs are at $210\ \text{MeV}/c$ and use the same amplifier with $50\ \Omega$ input impedance. “Y” and “N” designate the presence or absence of an extra header connector. The first four runs are at low gas gain, and the last four are at higher gas gain.

1835 V. The high gain voltage was chosen according to Sec. 2.3. Since our gain-doubling voltage is approximately 60 V, the low gain columns have about 84% the gain of the high gain columns. The voltages are higher than for the runs described in the earlier sections because the amplifiers have different electronic gain. The cable types 1855 and 179 are described in Sec. 2.4, while the Y and N designations indicate the presence or absence of the extra header connector, respectively.

A general trend to be noticed is that the high gain columns have noticeably better performance than the low gain columns, which is contrary to what was shown in Sec. 6.4. This is likely because these amplifiers have different electronic gains and the selected wire voltages do not lie in the same performance region as the results shown in Sec. 6.4.

The cable type and the inclusion of the header connector only marginally affect the figure of merit, by an amount less than the typical variation between identical runs and from the track composition process $\sim 5\%$. It is tempting to see that the 179N columns are the highest between the two sets, but the difference is not nearly as dramatic as the variation due to gas gain or the additional contribution of cluster counting itself.

6.8. Amplifiers

As described in Sec. 2.2, we tested several types of amplifiers, mostly distinguished by their input impedance and gain. We remind the reader that the sense wire voltages used are different for the various amplifiers, and were chosen to get approximately constant signal amplitude as described in Sec. 6.4.

In Fig. 27, the results from three different amplifiers at two different positions along the sense wire are shown. The input impedance of each amplifier is indicated, and the amplifiers with the same labels are the same for the two different positions. The $370\ \Omega$ “inv” amplifier returns an inverted signal, while the others do not.

There is considerable variation between the amplifiers, but the general result is that the $370\ \Omega$ amplifiers give the best results. This indicates the importance of matching the amplifier input impedance with the impedance and termination of the drift chamber

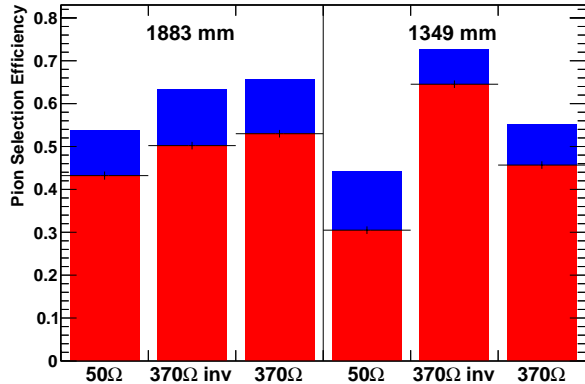


Figure 27: Variation in PID performance using different amplifiers. The red is the performance using charge integration only, the blue is the additional performance gain from combining charge integration and cluster counting. The upper labels indicate the beam position along the sense wire, measured from the amplifier. The “inv” label indicates an inverting amplifier.

itself. Unfortunately the indication of the best amplifier is not very strong, as a proper study of the optimal gas gain for each amplifier was not done in this experiment. The variation between the amplifiers in Figure 27 is of the same order as the variation with gas gain for a single amplifier shown in Figure 23. It is possible that the variations seen here are mostly due to gain effects rather than the impedance and implementation details of the amplifiers.

6.9. Summary of Results

The studies undertaken attempt to explore a multidimensional parameter space, so the results are difficult to summarize concisely. Here we restate the lessons learned from each study described above.

The various cluster counting algorithms all perform roughly equivalently (Sec. 6.2). Their parameters must be optimized for good performance, but the regions of good performance in parameter-space are quite large. Even sub-optimal parameters only give slightly worse performance. More advanced techniques (such as the timeout booster) can compensate for a less-optimized algorithm, but are unnecessary when the algorithm is optimized properly.

Optimal smoothing for the cluster-counting algorithms is on the order of a few nanoseconds, indicating that a higher sampling rate is unnecessary. The corresponding Nyquist frequency is on the order of hundreds of MHz. This means that the successful implementation of cluster counting does not depend on getting overly expensive or customized hardware. Indeed the best algorithm studied simply applies a threshold to the second-derivative of the signal, a process that can be done with analog electronics or in an FPGA.

Cluster timing gives results that are slightly poorer than cluster counting used alone (Sec. 6.3). When combined with charge integration and cluster counting however, the improvement is minor compared to charge integration and cluster counting without the cluster timing. Given the additional complexity of storing and calculating average cluster timings, this technique is unlikely to be worth exploring further.

PID performance depends strongly on having the proper wire voltages and thus gas gains (Sec. 6.4). In some configurations, higher gain is not necessarily better, but this is dependent on the choice of amplifier. Thus for a given amplifier and equipment configuration, the optimal gas gain must be carefully determined.

There is not much variation in PID performance as a function of the beam position along the sense wire length (Sec. 6.6). Since the signal is attenuated while travelling along the sense wire, this effect is coupled with the gain of the amplifier and the choice of wire voltages.

The choice of cable types and additional connectors seems to have a negligible effect on the PID performance (Sec. 6.7). Performance is very sensitive to the choice of amplifier (Sec. 6.8), but this is coupled with the sense wire voltage. There is a weak indication that matching the amplifier input impedance with the impedance and termination of the chamber itself gives better performance.

7. Conclusions

The general result is clear: implementing cluster counting increases the particle identification capability of a drift chamber. We make no claim of hav-

ing found the optimal equipment and analysis techniques in the multidimensional parameter space that we explored. Thus we can state that cluster counting improves PID performance even in sub-optimal conditions.

The absolute improvement in the pion selection efficiency at 90% muon rejection is generally around 10% (e.g. from 50% to 60%, and see Fig. 19). The improvement is greatest when the PID performance from charge integration only is poorest, thus making the detector PID response more uniform.

The optimal smoothing times for cluster-counting algorithms are on the order of a few nanoseconds, corresponding to a Nyquist frequency of hundreds of MHz. Thus successful cluster counting can be accomplished even with modest hardware.

All future particle physics experiments that use a drift chamber for PID should strongly consider a cluster-counting option. This study shows that performance gains can be obtained that justify the additional complexity and cost of a cluster-counting drift chamber.

Acknowledgements

This work was supported by the Natural Sciences and Engineering Research Council of Canada and TRIUMF. We thank Jerry Va'vra for lending us the MCPs for our TOF system, and Hirosiha Tanaka for lending us the oscilloscope for our Data Acquisition.

We thank Wyatt Gronnemoose and Steven Robertson for their assistance during the beam test.

The analysis made extensive use of open-source software: ROOT[13], Python[16], IPython[17], PyROOT[18] and NumPy[19].

A. Cluster-Counting Algorithms

Here are contained precise definitions of the cluster-counting and smoothing algorithms used in this work. We define a signal or trace as a series of voltage samples indexed by a discrete time variable $V(t)$. Though the time variable has units (in our raw format the units are 50 ps), here we treat it as an integer index. In general, a signal will have N samples indexed with integer t running from 0 to $N - 1$.

A.1. Smoothing Procedures

Two types of smoothing are used in the algorithms. One involves replacing each element of the signal by the average of itself and its neighbours, without reducing the total number of elements. The other reduces the total number of elements, and each element's value is the average of a set of elements in the original signal.

A.1.1. Boxcar Smoothing

The so-called “boxcar smoothing” with n frames substitutes each sample with the average of itself and the previous $n - 1$ samples. The first n samples (0 to $n - 1$) are a boundary case, replaced simply by $\tilde{V}_n(n)$.

$$\tilde{V}_n(t) = \begin{cases} \frac{1}{n} \sum_{i=0}^{n-1} V(t-i) & t \geq n, \\ \tilde{V}_n(n) & t < n. \end{cases} \quad (3)$$

A.1.2. Averaging

The so-called “true averaging” procedure produces a signal with a reduced number of samples. For an n -frame averaging, the result is a series of $k = N \div n$ voltages (floored division), indexed with the integer \bar{t} running from 0 to k .

$$\bar{V}_n(\bar{t}) = \frac{1}{n} \sum_{i=0}^{n-1} V(s + n\bar{t} + i) \quad (4)$$

Here, n is the number of samples that are averaged, $s = N \bmod n$, and N is the total number of samples in the original trace.

This averaging has the potential to “divide” cluster signals if the averaging bin edges lie on top of a cluster (Fig. 15). Thus it is useful to also shift the smoothing bins by adding $n \div 2$ to the argument of V inside the sum. If the smoothing is done with and without the shift, it is less likely that the same cluster will be divided in both cases, compared to doing the smoothing only one way.

A.2. Signal above Average

This algorithm has two parameters: a number of frames for smoothing and a threshold. From the non-smoothed signal at time t is subtracted the n -frame

smoothed signal at time $t - 1$. If the resulting quantity crosses the threshold Δ downwards, a cluster is identified at that time.

The cluster times found by this algorithm are those t in $\{\max(n, 2)..N\}$ that satisfy

$$\begin{aligned} (V(t) - \tilde{V}_n(t-1) < \Delta) \text{ and} \\ (V(t-1) - \tilde{V}_n(t-2) \geq \Delta). \end{aligned} \quad (5)$$

A.3. Smooth and Delay

This algorithm has four parameters: two smoothing times, a delay, and a threshold.

Two copies of the original signal are smoothed by different amounts (p and q frames) using the “boxcar smoothing”. The q -frame smoothed copy is then delayed by d frames, and the two copies are then subtracted. If the resulting quantity crosses the threshold Δ downwards, a cluster is counted at that time.

The cluster times found by this algorithm are those t in $\{d..N\}$ that satisfy

$$\begin{aligned} \frac{\tilde{V}_p(t) - \tilde{V}_q(t-d)}{d} < \Delta \text{ and} \\ \frac{\tilde{V}_p(t-1) - \tilde{V}_q(t-1-d)}{d} \geq \Delta. \end{aligned} \quad (6)$$

The “Signal above Average” algorithm is a special case with $p = 1$, $q = n$, and $d = 1$. Another special case can be constructed with $d = 0$ with the denominator set to 1.

It can be shown that if the two smoothing times are equal ($p = q$), the quantity computed with smoothing q and delay d is identical to that computed with smoothing d and delay q . Thus the parameter range can be restricted to $d > q$ without loss of generality.

A.4. Second Derivative

This algorithm has two parameters: a smoothing time and a threshold. It uses the true averaging procedure rather than the “boxcar smoothing”, so the time is labelled \bar{t} as in Sec. A.1.2. Simply put, the second derivative is calculated and compared with a threshold.

The second derivative is calculated as follows:

$$\bar{V}''(\bar{t}) = \frac{1}{\delta^2} \left([\bar{V}(\bar{t}+2) - \bar{V}(\bar{t}+1)] - [\bar{V}(\bar{t}+1) - \bar{V}(\bar{t})] \right) \quad (7)$$

where δ is the time interval corresponding to the n samples that were averaged to do the smoothing.

The times of the clusters found with the second-derivative algorithm are those \bar{t} in $\{0..N \div n\}$ that satisfy

$$\bar{V}''(\bar{t}) < \Delta \text{ and } \bar{V}''(\bar{t} - 1) \geq \Delta. \quad (8)$$

Because this algorithm uses the true averaging, it suffers from the problem of potentially “dividing” cluster signals between smoothing bins (Fig. 15). Thus we also implemented a two-pass second-derivative algorithm that looks for clusters a second time on the averaged signal with a delay applied as described in Sec. A.1.2. The numbers of clusters found in each pass are added together. It is understood that the resulting cluster count is inflated because many clusters will be double-counted, but nevertheless it is an appropriate variable for identifying particles.

A.5. Timeout Booster

The so-called “timeout booster” takes as an input the list of clusters found by one of the above algorithms. It considers these as cluster candidates, and validates or rejects each one in turn.

For a given cluster candidate, the voltage and time in the original waveform at which the cluster-finding algorithm was triggered is recorded. Then following the waveform forward, the voltage is checked to see when it has recovered above the recorded value (the pulses are negative). If the voltage recovered within the timeout window, it is a short-lived pulse and thus rejected as a fake. If the timeout is reached without the voltage recovering, it is long-lived and kept as a real cluster.

For a list of potential clusters t'_i , real clusters satisfy

$$V(t) < V(t'_i) \text{ for all } t \text{ in } \{t'_i..(t'_i + T)\} \quad (9)$$

where T is the chosen timeout. The rejection of fake clusters by the timeout procedure permits the use of lower thresholds in the original algorithm. The lower threshold increases the efficiency of finding real clusters (smaller miss rate) but increases the rate of

detecting fake clusters. The timeout procedure then eliminates most of the fake clusters, keeping the real ones.

References

- [1] A. H. Walenta, “The Time Expansion Chamber and Single Ionization Cluster Measurement,” *IEEE Trans. Nucl. Sci.*, vol. 26, no. 1, pp. 73–80, 1979.
- [2] M. Bona *et al.* (SuperB Collaboration), “*SuperB*: A High-Luminosity Asymmetric $e^+ e^-$ Super Flavor Factory. Conceptual Design Report,” *arXiv:0709.0451*, Sep. 2007.
- [3] E. Grauges *et al.* (SuperB Collaboration), “SuperB Progress Reports – Detector,” *arXiv:1007.4241*, July 2010.
- [4] M. Baszczyk *et al.* (SuperB Collaboration), “SuperB Technical Design Report,” *arXiv:1306.5655*, June 2013.
- [5] G. Charpak, R. Bouclier, T. Bressani, J. Favier, and Č. Zupančič, “The use of multiwire proportional counters to select and localize charged particles,” *Nucl. Instrum. Meth.*, vol. 62, no. 3, pp. 262–268, 1968.
- [6] W. Blum, W. Riegler, and L. Rolandi, *Particle Detection With Drift Chambers*. Springer, 2008.
- [7] H. Bethe, “Zur theorie des durchgangs schneller korpuskularstrahlen durch materie,” *Annalen der Physik*, vol. 397, no. 3, pp. 325–400, 1930.
- [8] J. Beringer *et al.* (Particle Data Group), “Review of Particle Physics,” *Phys. Rev. D*, vol. 86, Jul 2012.
- [9] B. Aubert *et al.* (BaBar Collaboration), “The BaBar detector,” *Nucl. Instrum. Meth.*, vol. A479, pp. 1–116, 2002.
- [10] P. Burchat, J. Hiser, A. Boyarski, and D. Briggs, “Studies of helium gas mixtures in drift chambers,” *Nucl. Instrum. Meth.*, vol. A316, pp. 217–222, 1992.
- [11] R. Veenhof, “Garfield, recent developments,” *Nucl. Instrum. Meth.*, vol. 419, no. 2-3, pp. 726–730, 1998.
- [12] E. Blackmore, “Operation of the TRIUMF (20-500 MeV) proton irradiation facility,” in *IEEE Radiation Effects Data Workshop*, 2000.
- [13] R. Brun and F. Rademakers, “ROOT — An object oriented data analysis framework,” *Nucl. Instrum. Meth.*, vol. 389, no. 1-2, pp. 81–86, 1997.
- [14] S. Ritt and P. A. Amaudruz, “The MIDAS Data Acquisition System,” <http://midas.triumf.ca>, 2002.
- [15] D. N. Poenaru and W. Greiner, *Experimental Techniques in Nuclear Physics*. De Gruyter, 1997.
- [16] G. Van Rossum, *The Python Language Reference Manual*. Network Theory Ltd., Sept. 2003.
- [17] F. Pérez and B. E. Granger, “IPython: a System for Interactive Scientific Computing,” *Comput. Sci. Eng.*, vol. 9, no. 3, pp. 21–29, 2007.
- [18] J. Generowicz, W. Lavrijsen, M. Marino, and P. Mato, “Reflection-Based Python-C++ Bindings,” in *Computing in High Energy and Nuclear Physics (CHEP)*, 2004.
- [19] S. van der Walt, S. Colbert, and G. Varoquaux, “The NumPy Array: A Structure for Efficient Numerical Computation,” *Comput. Sci. Eng.*, vol. 13, no. 2, pp. 22–30, 2011.